

## RESEARCH ARTICLE

10.1002/2014JF003304

## Key Points:

- Examine the probabilistic structure of incremental drainage area
- Relate the main stem incremental area function to the width function
- Quantify the spatial heterogeneity of environmental fluxes

## Correspondence to:

C. Gangodagamage,  
chhandana@gmail.com

## Citation:

Gangodagamage, C., E. Fofoula-Georgiou, and P. Belmont (2014), River basin organization around the main stem: Scale invariance in tributary branching and the incremental area function, *J. Geophys. Res. Earth Surf.*, 119, 2174–2193, doi:10.1002/2014JF003304.

Received 4 AUG 2014

Accepted 15 SEP 2014

Accepted article online 17 SEP 2014

Published online 13 OCT 2014

## River basin organization around the main stem: Scale invariance in tributary branching and the incremental area function

Chandana Gangodagamage<sup>1,2</sup>, Efi Foufoula-Georgiou<sup>2</sup>, and Patrick Belmont<sup>2,3</sup>

<sup>1</sup>Earth and Environmental Sciences Division, Los Alamos National Laboratory, Los Alamos, New Mexico, USA, <sup>2</sup>St. Anthony Falls Laboratory and National Center for Earth-surface Dynamics, Department of Civil Engineering, University of Minnesota, Twin Cities, Minneapolis, Minnesota, USA, <sup>3</sup>Department of Watershed Sciences, Utah State University, Logan, Utah, USA

**Abstract** The incremental increase in contributing area along a main stem river, called here the incremental area function (IAF), has direct relevance to the spatial heterogeneity of environmental fluxes (water, sediment, nutrients, etc.) entering the stream from hillslopes and side tributaries. It also dictates, to a large extent, possible ecohydrologic discontinuities or transitions resulting from large tributary contributions. Mathematically, the IAF directly reflects the topological and geometrical structure of the river network and maps the two-dimensional landscape organization into a one-dimensional function. In this paper, we use two approaches to investigate the spatial heterogeneity of the IAF. First, we implement a multithreshold decomposition on IAF to study the distribution of distances between tributaries as a function of the imposed threshold contributing area and verify the presence of a simple power law scaling relationship between the threshold and the average distance between tributaries. Second, we use a wavelet-based multiscale approach and document the presence of statistical self-affinity (multifractality) in the IAF with a high intermittency coefficient, reflecting the complex arrangement of extreme contributions of different size tributaries. We propose a multiplicative cascade model, parameterized in terms of basin-specific properties, to statistically simulate the IAF along the main stem. Finally, we point out the relation between the IAF and the widely used width function of a basin and show how the latter can be constructed from the former via a convolution on the self-similar structure of a tree.

### 1. Introduction

Tributary junctions are important bottlenecks for floods, points of sudden increase in sediments, nutrients, and pollutants [e.g., *Riveros-Iregui et al.*, 2011; *Richards-Pecou*, 2002] and also regions of morphologic and ecological discontinuities and transitions [e.g., *Benda et al.*, 2004a, 2004b; *Convertino et al.*, 2007; *Jencso and McGlynn*, 2011; *Caylor et al.*, 2006; *Beechie and Imaki*, 2014]. As such, the hierarchical structure of tributary junctions deserves focused attention, especially in terms of understanding their influence on the downstream propagation of fluxes and the emergence of transitions in environmental regimes. For example, sudden tributary influx of sediments into the main stem changes its longitudinal profile over time and influences channel size and bed morphology, river corridor width, bed material size, riparian vegetation, and river biotic life [e.g., *Jenson and Domingue*, 1988; *Rodriguez-Iturbe and Rinaldo*, 1997; *Rice*, 1998; *Benda et al.*, 2004a; *Kiney et al.*, 2006; *Ferguson et al.*, 2006; *Convertino et al.*, 2007; *Gangodagamage et al.*, 2007; *Gangodagamage*, 2009; *Gangodagamage et al.*, 2011; *Muneepeerakul et al.*, 2007a, 2007b, 2008; *Rice et al.*, 2008; *Tarolli*, 2014; *Duncan et al.*, 2007; *Rodriguez-Iturbe et al.*, 2009]. Assuming that fluxes are proportional to the area that generates them, an improved quantification of the geometrical and statistical structure of the changes in contributing drainage area along the main stem of a river from fine (i.e., hillslope scales at resolutions of 1–10 m) to coarse scales (i.e., whole river basins at resolutions of 1–10 km) will produce additional insight into the organization of landscapes as it relates to the spatial heterogeneity and statistical scaling of water, nutrients, and other fluxes [e.g., *Rodriguez-Iturbe et al.*, 2009; *Riveros-Iregui et al.*, 2011; *Jencso and McGlynn*, 2011; *Duncan et al.*, 2007; *Ferguson et al.*, 2006; *Gangodagamage et al.*, 2014, among others]. Significant tributary junctions, i.e., large peaks in the incremental area function (IAF), mark points of highly dynamic transitions in terms of ecohydrological functioning, as they affect the flow of energy and species behavior with important implications for the functioning of food webs [e.g., *Power*, 1992; *Ward et al.*, 2002; *Wiens*, 2002; *Benda et al.*, 2004b].

The spatial variability of the upstream contributing area and incremental contributing area along channel networks has been an important model parameter for water quality as well as transfer and migration of organisms across the landscape [Alexander *et al.*, 2000; Gangodagamage *et al.*, 2008; Kirchner and Neal, 2013; Rinaldo *et al.*, 2014; Banavar *et al.*, 2014]. Spatially varying dispersion terms, such as hydrodynamic or kinematic dispersion, as a function of contributing area have also been extensively studied [Saco and Kumar, 2002; Snell and Sivapalan, 1994; Rinaldo *et al.*, 1991]. Incremental drainage area was also used to predict total nitrogen load along the Mississippi River [Alexander *et al.*, 2000]. However, only a few existing formulations explore the abrupt fluctuations (sudden changes in contributing area) introduced by side tributaries at network junctions [e.g., Convertino *et al.*, 2007]. Lateral fluxes, which drain to the main stem from the left and right sides, reflect the hierarchical organization and branching topology of the river network, are governed by the scale-dependent lateral organization of the tributaries and capture the sudden change of contributing area at tributary junctions which materializes over very small length scales. Recent availability of high-resolution lidar digital terrain data (1 m resolution from light detection and ranging) offers the opportunity to study in detail the structure of the contributing areas as one moves down the main stem channel, both in terms of its high-frequency (abrupt changes at small scales) and low-frequency (average trends over larger scales) components.

The focus of this paper is the incremental area function (IAF), which we define as follows:

$$\text{IAF}(x; dx) = A(x + dx) - A(x), \quad (1)$$

where  $x$  is distance along the main stem starting at the drainage divide ( $x=0$  at the divide and  $x=L$  at the basin outlet),  $A(x)$  is the upstream contributing area at distance  $x$  from the divide, and  $dx$  has the notion of "scale." We explore the statistical properties of the IAF as a function of scale and show that it exhibits stochastic-scale invariance (multifractality), carrying thus the signature of the extended hillslope-river network topology. We present results for three nested river basins and demonstrate the connection of IAF to the well-studied width function of a basin.

## 2. Basins Analyzed and Extraction of IAF

Extraction of the IAF is performed on a digital elevation model (DEM) by following the largest flow accumulation along the principal flow path from the outlet to divide. Flow accumulation is computed using the simple eight-cell, neighbor-based D8 flow-direction algorithm [O'Callaghan and Mark, 1984], that is, by accumulating the contributing area along the slopes of steepest descent. The D8 algorithm was used for computational efficiency, as we tested the algorithm with D-inf [Tarboton, 1997] and obtained very similar results. A hydrologically connected DEM is used by filling flat areas and local depressions [Jenson and Domingue, 1988; Hutchinson, 1989; Reiger, 1998] in the DEM. The percentage of pits that we had to fill varied from 0.02% to 0.07% by considering 2 km by 2 km tiles covering the entire 354 km<sup>2</sup> SF-Eel River basin. We initially demarcated the main stem as the flow path with the largest flow accumulation, moving upstream from the outlet to the ridge crest. This channel will often, but not always, be the longest flow path in the basin. From the basin outlet we ran an algorithm that considers pixels along the main stem between the basin outlet (at distance  $L$  from the drainage divide) and 100 m from the drainage divide (identified as the transition point from divergent topography (hillslope) to convergent (fluvial-dominated) topography, per Gangodagamage *et al.* [2011]). On hillslopes (less than 100 m from the drainage divide), the IAF was computed as an ensemble average of contributing area as a function of the distance measured from the drainage divide. Then, we extracted the incremental contributing area along the main stem from distance  $x=0$  (at the drainage divide) to the distance  $x=L$  (at the outlet). The IAF is extracted at each 1 m pixel moving progressively downstream along the main stem. Thus, it depicts the lateral contribution of the hillslopes and tributary basins joining from the right and left down to the meter scale, with large, discrete spikes occurring at tributary junctions. Here we note that the length scale associated with a spike in the IAF occurs at a 1 m grid. However, in reality, this IAF fluctuation is a function of the tributary channel width which can range from 5 to 15 m in the SF-Eel River basin [Gangodagamage *et al.*, 2007]. It is important to mention here that the IAF can also be generated using coarse grid resolution DEMs (e.g., 30 m grid resolution), in which case the resolution (smallest scale) of the IAF is equal to the contributing area represented by a single grid cell (e.g., in the case of 30 m data,  $\text{IAF} < 900 \text{ m}^2$  will not be represented). This concept is explored more in section 4.1.

Three basins were used in this analysis. These are the South Fork Eel River basin (area of 354 km<sup>2</sup> and main stem length  $L = 56.6$  km) and two nested subbasins, Elder Creek basin (area of 18 km<sup>2</sup> and  $L = 11.2$  km)

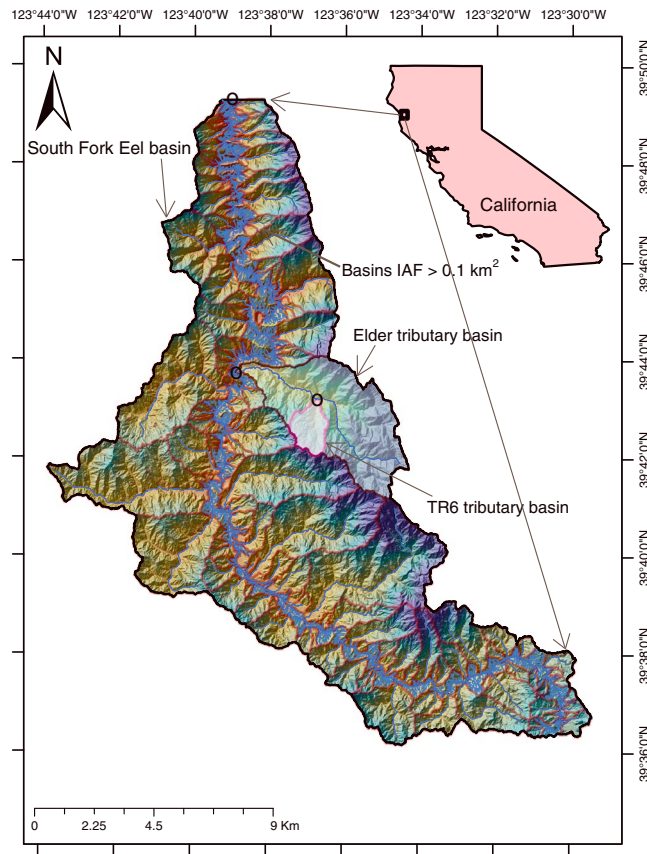


**Figure 1.** The South Fork Eel River basin (area of 354 km<sup>2</sup>, dot indicates the outlet of the basin) and two of its subbasins the Elder tributary basin (18 km<sup>2</sup>) and TR6 basin (3 km<sup>2</sup>) are shown. The location of the SF-Eel River basin in Northern California is shown in the inset map.

and a subbasin of Elder known as TR6 (area of 3 km<sup>2</sup> and  $L = 2.8$  km). These basins are shown in Figure 1. The South Fork Eel River basin sits within the tectonically active 70 km wide zone of deformation known as the San Andreas Fault zone [Kelsey and Carver, 1988]. The basin is underlain by Tertiary-Cretaceous Coastal Belt Franciscan clastic sedimentary rocks, primarily composed of arkosic sandstone, pebble conglomerate, and mudstone [Strand, 1962; Jennings and Strand, 1960]. Several transient knick zones have been identified in the basin that appears to be related to multiple instances of base-level fall [Foster and Kelsey, 2012].

Average gradient (total relief divided by total length) of the SF-Eel basin is 0.0097 m/m, while that of Elder Creek is 0.0852 m/m and that of TR6 is 0.2083 m/m. Other physiographic and geologic characteristics of those basins can be found in Seidl and Dietrich [1992], Gangodagamage et al. [2007, 2011], and Fuller et al. [2009]. The IAFs were computed for these basins and are shown in Figures 2b–2d. Figure 2a shows all the major subbasins of the SF-Eel River basin that contribute directly to the main stem, i.e., these are the basins that

form spikes in the IAF. Broken-line arrows indicate the areas that contributed to the spikes in the IAF, the largest of which is Elder Creek at a downstream distance of 32.4 km from the drainage divide. Looking at the IAF signals of Figure 2a, it is interesting to ask the question as to what statistical characteristics these signals possess. For example, do they exhibit scale invariance? Is their structure dependent on the basin size? How does the structure of the IAF relate to the fractality (self-affinity) of another well-studied function, i.e., the area or width function of a basin? How might the frequency, magnitude, and sequence of steps in the signal influence the dynamics of water, sediment, and nutrient transport as well as other ecological processes?

The cumulative IAF curves for the three basins (collapsed to a single plot via normalization) are shown in Figure 2e. The sudden jumps of various sizes in the magnitude of the signal occur at many different locations highlighting the important role that the nested arrangement of tributaries plays in dictating the cumulative fluxes along the main stem. For many processes, the distance (length scale) between such large contributions is important as it might relate to dilution of pollutants, bedload sediment accumulation, downstream sediment fining, etc. considerably affecting the state of the main stem as dictated by the overall basin contributions. It is important to note that the majority of the jumps in IAF are small (low-frequency content), and these small jumps are likely unimportant from a hydrogeomorphic-ecological perspective. What really matters are the larger jumps and the average distances between these large jumps.

### 3. Generation of the Width Function From the IAF

The IAF is a one-dimensional function that summarizes the two-dimensional topological (branching) and geometrical (link length) structure of the river network as mapped onto the incremental drainage areas

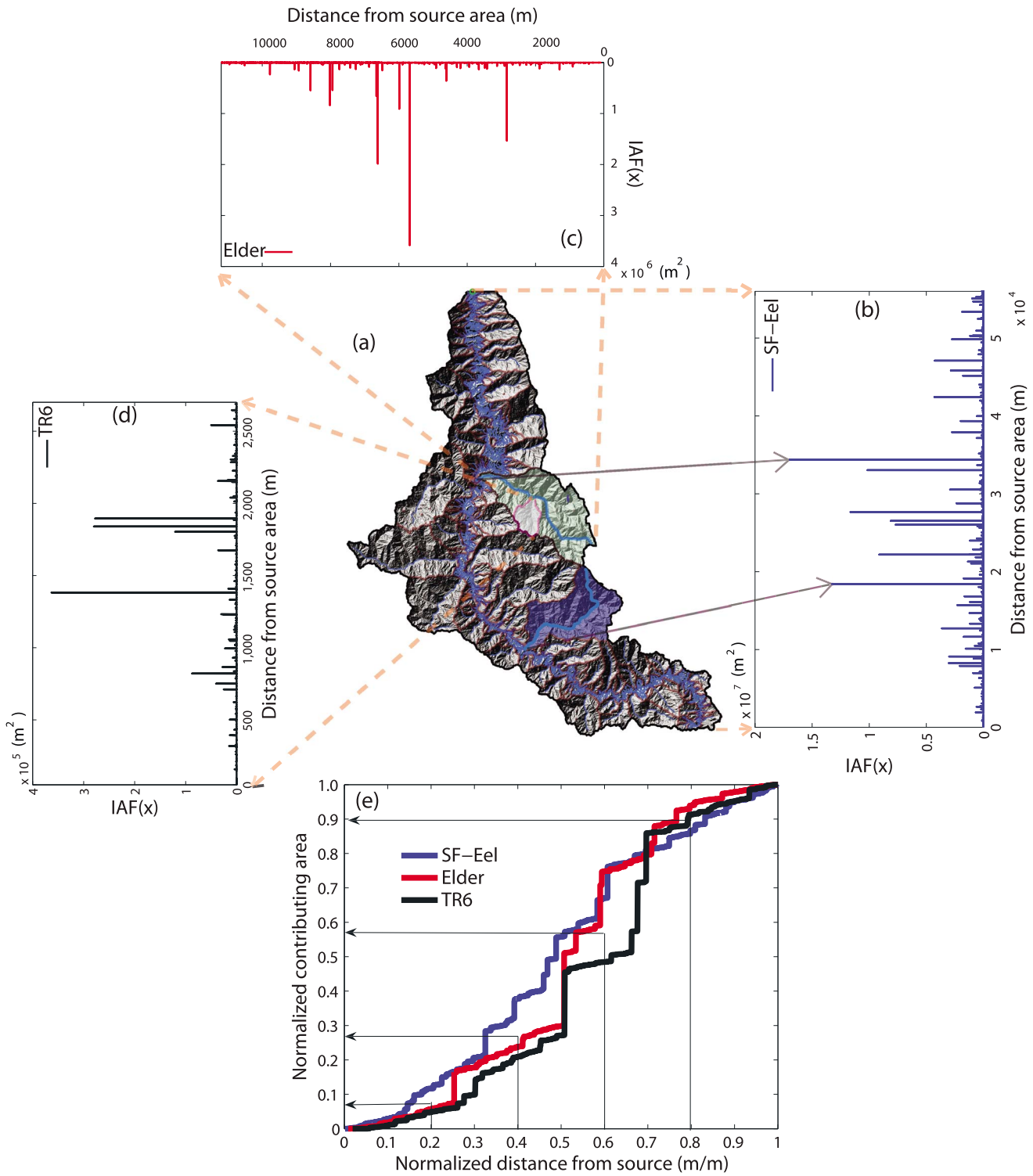


**Figure 2.** (a) The South Fork Eel River basin with all its tributaries draining directly to the main channel is shown. For illustration purposes, we have indicated that the two largest tributaries (shaded) map as large spikes in the incremental area function. Main stem lengths from drainage divide to outlet are 56.6 km, 11.2 km, and 2.8 km, respectively, for the (b) SF-Eel, (c) Elder, and (d) TR6 basins. (e) The normalized cumulative area function as one moves downstream along the main stem is plotted for each basin. Jumps in the functions indicate major tributaries. The horizontal arrows indicate the values of the normalized cumulative contributing areas used to derive the weights of the pentanomial cascade generator (see section 6).

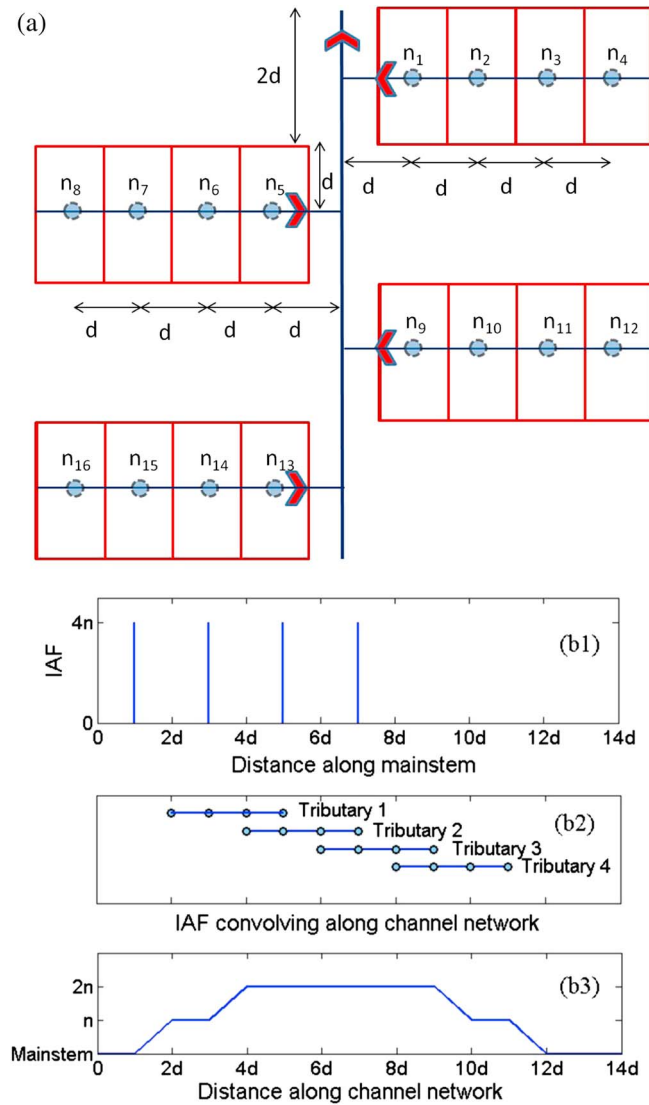


**Figure 3.** An illustration of generating the area function from the IAF. (a) Shows a hypothetical basin with four tributary basins. Each tributary basin again is divided into four rectangle subbasins each having a drainage area of  $n$  pixels ( $n_1 = n_2 = \dots, n_{16} = n$ ) located  $d$  or  $2d$  or  $3d$  or  $4d$  distances away measured from the main stem. The hillslope contribution is neglected. (b1) The IAF function of this basin is shown, where  $4n$  tributary contributions from each tributary basin joining to the main stem at  $2d$  distance apart. The first basin is located  $1d$  distance from the basin outlet. Horizontal lines indicate lengths over which IAFs are convolved. (b2) Area function is obtained by summing up the convolution of IAF with river network.

subbasin IAFs of all tributaries as they join the main stem. This is demonstrated via a simple example and via analysis of the real basins below.

An illustration for generating the area function from the IAF is given in Figure 3 using a very simple, hypothetical basin with four tributary basins (Figure 3a, Tributaries 1, 2, 3, and 4). Each tributary basin is again divided to four rectangular subareas with each having  $n$  number of pixels ( $n_1 = n_2 = \dots, n_{16} = n$ ) located at various distances ( $d, 2d, 3d,$  or  $4d$ ) measured laterally from the main stem. The main stem is attributed with distances for measurement, but contributes no additional drainage area. The IAF of this basin is shown in Figure 3b1, where  $4n$  tributary contributions from each basin join the main stem at distances apart equal to  $2d$ .

along the main stem. Another well-known one-dimensional function which summarizes the topological and geometrical structure of the river basin is the width function  $W(x)$  (or equivalently referred to here as the area function  $A(x)$ )—see Rodriguez-Iturbe and Rinaldo [1997] and also discussion in Lashermes and Foufoula-Georgiou [2007]). The width function is defined as the number of channelized pixels at a flow distance  $0 < x < L$  from the basin outlet, where  $L$  is the longest channelized path in the network, i.e., the main stem. The area function  $A(x)$  is defined as the number of pixels, not necessarily channelized at a flow distance  $x$  from the basin outlet, i.e., it captures the drainage area contributed to the outlet from a zone enclosed by the contours at distances  $x$  and  $x + dx$  from the basin outlet. Obviously,  $W(x)$  and  $A(x)$  relate to each other via a length-to-area transformation, which however, might differ among the fluvial and hillslope regimes. It is interesting to ask whether IAF(x) and  $W(x)$  are related to each other and how. In this section, we show that  $W(x)$  can indeed be reconstructed by an iterative process on the IAF(x) along the river network. Intuitively, this is explained as follows. First, we note that both the IAF and  $W(x)$  integrate to the total area of the basin. The IAF captures only the newly added fluxes along the main stem between locations  $x$  and  $x + dx$ , while the width function captures the integrated contributions from all the subbasins that contain flow paths at distances between  $x$  and  $x + dx$  from the outlet. As such, it is expected intuitively that the width function will result from a convolution (or integration) of the individual

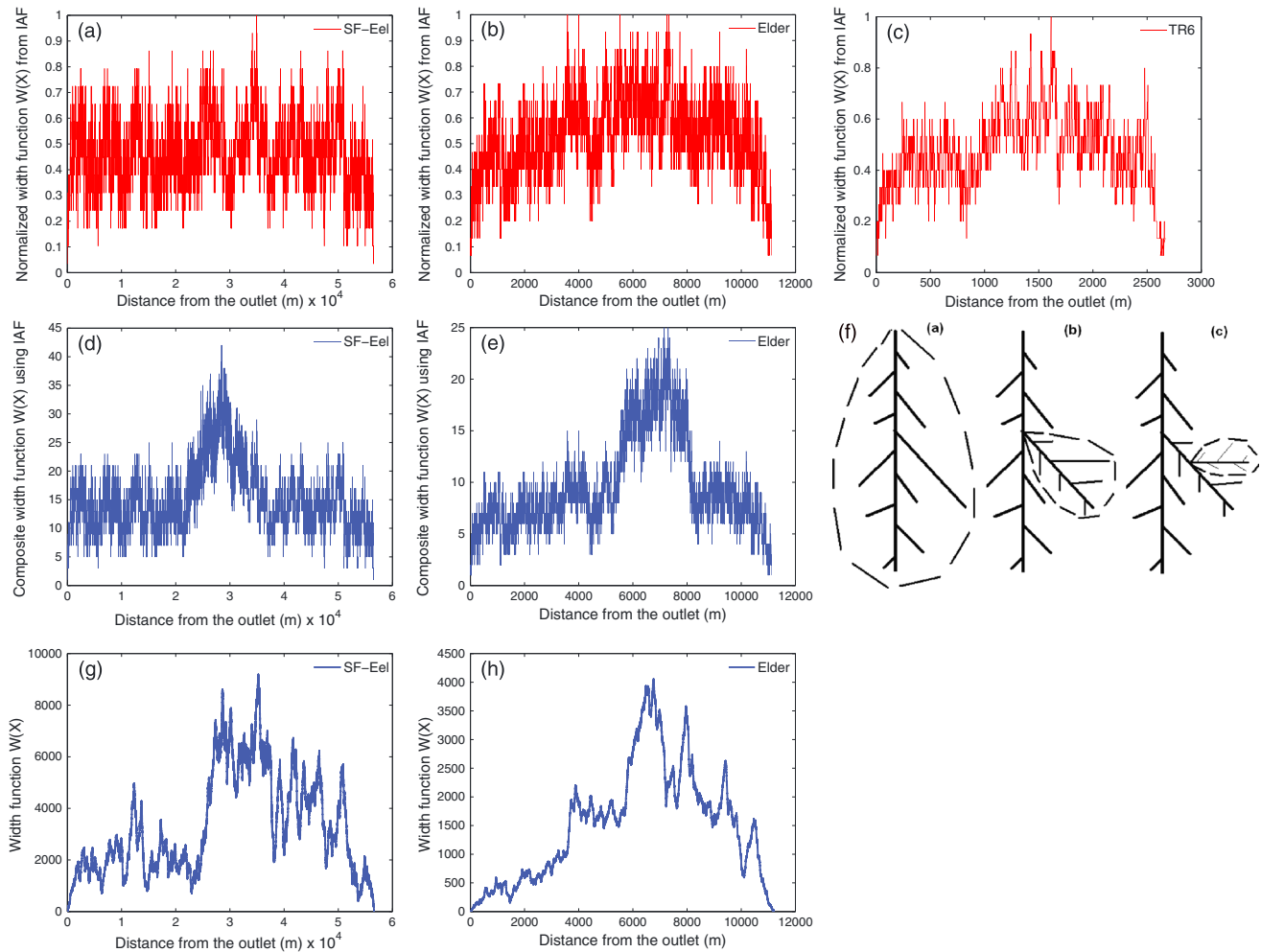


**Figure 4.** The top row shows the “rudimentary width functions” for the three basins, (a) SF-Eel, (b) Elder, and (c) TR6, obtained from the IAFs by a simple conversion of areas to lengths. The corresponding width functions after two iterations for the (d) SF-Eel and (e) Elder Creek basins are shown in the second row. (f) The schematic to the right illustrates the iterative convolution process for the generation of the  $W(x)$  from the  $IAF(x)$ . The independently derived width functions using directly the lidar data for those basins are shown at the bottom row for (g) SF-Eel and (h) Elder.

The first basin joins the main stem at a distance  $d$  from the basin outlet as shown in Figure 3b1. The IAF functions are convolved with the upstream lateral river network and then converted to the corresponding area functions (Figure 3b2). The area function of the whole basin is obtained by summing up the convolutions of IAF along the river network as shown in Figure 3b3.

Now we show the same approach for real basins. We start with the  $IAF(x)$  for the South Fork Eel as shown in Figure 1 (IAFs for SF-Eel, Elder, and TR6 basins). At each location  $0 \leq x \leq L$  along the main stem, we “convert” the incremental contributing area to an equivalent length using regional relationships generated by *Gangodagamage et al.* [2011]:  $A(l) \sim l^\theta$ , where  $\theta = 1.70$  for  $A \geq 1 \times 10^{-1} \text{ km}^2$  (channelized subbasins draining to the main stem),  $\theta = 3.10$  for  $1 \times 10^{-1} \geq A \geq 1 \times 10^{-4} \text{ km}^2$  (corresponding to convergent parts of the hillslope draining directly to the main stem) and  $\theta = 1.00$  for  $A \leq 1 \times 10^{-4} \text{ km}^2$  (corresponding to planar or divergent parts of the hillslope). It is noted that the effect of the exponents converting areas to length for the very small contributing areas corresponding to nonchannelized parts of the basin is not an issue of concern here as the iterative process pertains mostly to the larger tributaries for which the Hack’s area-length relationship applies (exponent  $\theta = 1.70$ ; see also discussion in section 6) [Hack, 1957]. This step results in a rudimentary “width function” for all three basins as shown in Figures 4a–4c (top row plots). We note that even if we used different Hack’s exponents to represent the area-to-length conversion along the various flow paths contributing to the main stem in different landscape regimes (i.e., divergent, hollows, and fluvial

regimes), these regime breaks are not universal because climate, lithology, tectonics, and previous glaciations can strongly influence the flow path lengths in different parts of a basin. A spatially variable drainage density index could possibly be incorporated to account in more detail for these different regimes in converting the IAF to the width function, something not pursued here.

At the location of the IAF where the largest tributary joins, we impose on that tributary its own IAF( $x$ ) (see schematic representation in Figure 4f, middle row right plot) and iterate once to refine the initial width function. For example, here we use the IAF for the TR6 basin to refine the rudimentary width function of the Elder Creek basin and subsequently the IAF of the Elder Creek basin to further refine the width function of the South Fork Eel. In that way, we compute revised width functions for those basins by convolving their initial rudimentary width functions (obtained directly by the IAFs) with those of their major subbasins. The result of the convolution is shown in Figures 4d and 4e (middle row plots). This process can be repeated hierarchically for other subbasins, leading each time to a refinement of the initial width functions to obtain, after many iterations, a close approximation to the real width functions as shown in Figures 4g and 4h (bottom row).

One can argue that instead of applying the real IAF( $x$ ) for each subbasin in that convolution process, one can either apply geometrically scaled versions (rescaled exact duplicates) of the main stem IAF for all subbasins or use the multiscaling properties of the IAF reported in the next section to generate synthetic versions of the IAFs. The latter would account for the natural variability in a landscape while preserving the general hierarchical clustering of tributaries. Such an approach would require a stochastic simulator of IAFs such that not only its multifractal properties are preserved but also ensure that other constraints imposed by the river network and shape of the river basin are satisfied. In section 6, we present such a stochastic simulator of IAF. We note here that a cascade simulator that distributes the effects of forcing uniformly throughout the basin, as opposed to preferentially along selected stretches of the main stem, will dilute the effects of the anisotropic drivers (i.e., not sufficiently spatially represented in places where they are actually present and may be represented in places where, in actuality, they are not). Hence, in such a case the synthetic IAF may not generate spatial heterogeneity in a geologically sensitive way. It may, nevertheless, still provide a useful way to generate a generic stream network with uniform scaling properties.

#### 4. Multiscale Analysis of IAF

The magnitudes and the distances between IAF spikes are important controls on hydrogeomorphic and ecological processes in river networks. To quantify the frequency and range of these spikes as well as their spatial distribution, we use a multithresholds and multifractal (MF) analysis. Before the results of this analysis are presented, we give a brief summary of our methodology. In section 4.1 we explore how IAF is related to the average distance between large tributaries, and in section 4.2 we explore the scale-dependent influences of IAF along the main stem.

##### 4.1. Multithreshold Decomposition of IAF: Distance Between Tributaries

Large tributaries occupy space and the distance between two large tributaries is larger when they join from the same side than from opposite sides along the main stem. This distance between tributaries as a function of the side tributary contributing area plays significant role in species distribution across different riverine ecosystems [e.g., Banavar *et al.*, 2007; Muneepeerakul *et al.*, 2007a]. It is also an important parameter for ecological processes, which fundamentally depend on the fluctuations in streamflow (master variable) due to the structure of tributary areas along the main stem. The original IAF series included the side tributary contributing areas from the smallest flow paths (i.e., a single pixel) to the largest tributary (IAF<sub>max</sub>) basin. By choosing a threshold value IAF <sub>$t$</sub>  and keeping only values of the IAF( $x$ ) above that threshold, a new series is produced, denoted as IAF <sub>$t$</sub> ( $x$ ). For example, by applying the threshold value of IAF <sub>$t$</sub>  = 2 m<sup>2</sup> (i.e., 2 <sup>$i$</sup> ,  $i = 1$ ) a new series was obtained by removing all the IAF values that are lower than 2 m<sup>2</sup>. Other IAF <sub>$t$</sub>  values were chosen by changing  $i$  from 1 up to log<sub>2</sub>(IAF<sub>max</sub>) in increments of one, where IAF<sub>max</sub> was the largest tributary basin. This approach provided multiple series that exceed the given threshold IAF <sub>$t$</sub>  along the main stem.

The inverse function of IAF <sub>$t$</sub> ( $x$ ) (i.e., IAF <sub>$t$</sub> <sup>-1</sup> =  $X(\text{IAF} > \text{IAF}_t)$ ) provided the incremental distance  $d_{\text{IAF}_t}$  for a given threshold value along the main stem from the divide to the basin outlet. By varying the value of the threshold, we computed the mean distances between tributaries and flow paths exceeding a given area along the main stems of the SF-Eel, Elder, and TR6 basins. The standard deviation of the distance ( $d_{\text{IAF}_t}$ )

between tributary inputs exceeding a given threshold area was also computed to capture the variability of the distances between tributaries.

#### 4.2. Multiscale Wavelet Decomposition on IAF

A multifractal function can be seen as a collection of local singularities (spikes), whose strength is characterized by the Hölder exponent. The local Hölder exponent  $h(x_0)$  at location  $x_0$  is defined as [e.g., Feder, 1988; Muzy et al., 1994] follows:

$$|A(x) - A(x_0)| \sim |x - x_0|^{h(x_0)} \quad (2)$$

for  $|x - x_0| \leq \varepsilon$ . Here  $\varepsilon$  is an infinitesimal distance along the main stem. This definition holds for  $0 \leq h \leq 1$  but is easily extended to  $h > 1$  by appropriate filtering (e.g., see Arneodo et al. [1995] and also Venugopal et al. [2006]). A small value of  $h$  indicates a more irregular function ( $h = 0$  corresponds to a discontinuity, e.g., a step function), while a larger value of  $h$  indicates a smoother function. For a multifractal function, the local Hölder exponents  $h(x_0)$  are assumed to be spatially distributed on interwoven fractal sets:

$$S(h) = \{x_0 : h(x_0) = h\} \quad (3)$$

where  $S(h)$  is the collection of points with Hölder exponent  $h$ . An efficient way to characterize multifractal functions is by using the Hausdorff dimension of the subsets  $S(h)$  [e.g., Schroeder, 1991], i.e.,

$$D(h) = \text{Dim}_H S(h) \quad (4)$$

The function  $D(h)$  is called the singularity spectrum and characterizes here the “degree of singularity” or the strength of the isolated IAF peaks arising from large incremental areas  $A(x) - A(x + dx)$  as tributaries and hillslopes join the main stem.

Monofractal functions have the same degree of singularity throughout their range and thus the Hölder exponent ( $h$ ) takes the same value  $H$  everywhere. In this case, the singularity spectrum reduces to a single point:  $D(h) = 1$  if  $h = H$  and  $D(h) = -\infty$  if  $h \neq H$ . For multifractal functions,  $D(h)$  spans a range of Hölder exponents from  $[h_{\min}$  to  $h_{\max}]$  and the “width” of  $D(h)$  is a measure of the heterogeneity of the singularities present in the signal.

It is noted that the wavelet-based multifractal formalism used here applies to both singular measures (defined only via integration, as for example, a Dirac delta) [Venugopal et al., 2006] as well as functions. Thus, it encompasses adoptively both the “sum in boxes” as well as the “increments” analysis methodologies (see Venugopal et al. [2006] and Lashermes and Foufoula-Georgiou [2007] for details). If the process under consideration is a singular measure (such as the IAF we consider herein), it suffices to work with the integral of this measure and shift the estimated  $D(h)$  spectrum to the left by 1, since differentiation reduces the singularity order by 1, as long as the function does not possess oscillatory singularities [Arneodo et al., 1995]. This issue will be discussed again in the next section and Appendix A.

#### 4.3. Estimation of $D(h)$ via Continuous Wavelet Transform (CWT)

$D(h)$  is estimated from the basin-wide statistics of the local fluctuations of the tributaries and hillslopes at different scales and at different locations  $x_0$  along the main stem. As extensively discussed in Venugopal et al. [2006] and Lashermes and Foufoula-Georgiou [2007], there are several advantages in using wavelet filtering to define the local fluctuations of a function. In fact, a wavelet-based multifractal analysis provides a robust framework for the estimation of  $D(h)$ , which encompasses both the box counting method (adequate for stationary measures) and higher-order differencing for nonstationary functions for which first-order increments do not remove trends present in the signal. Pitfalls that can arise from the selection of inappropriate filtering and example applications to known signals can be found in Lashermes and Foufoula-Georgiou [2007]. In this work, we adopt the wavelet-based multifractal formalism for the estimation of  $D(h)$ , which is briefly summarized below. Let the increments of the function  $A(x)$  at a scale  $a$  and location  $x_0$  be defined as follows:

$$\delta(x_0, a) = \int \psi_{x_0, a}(x) A(x) dx \quad (5)$$

where  $\psi_{x_0, a}(x)$  is a scale-dilated and shifted version of the mother wavelet:

$$\psi_{x_0, a}(x) = \frac{1}{|a|} \psi_0\left(\frac{x - x_0}{a}\right) \quad (6)$$

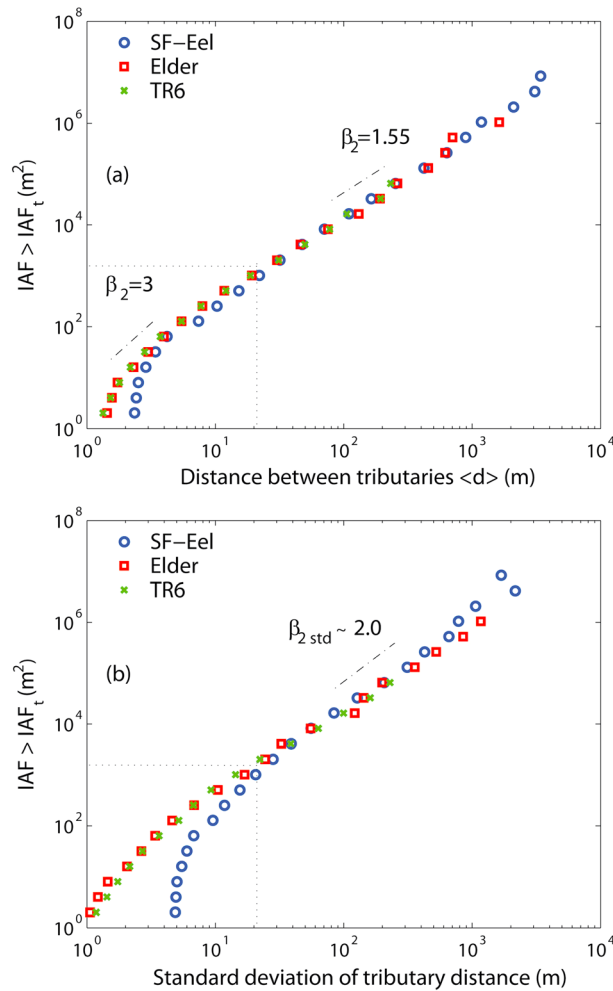


**Figure 5.** (a) The mean distance between tributaries and flow paths  $\langle d_{IAF_t} \rangle$  plotted against the  $IAF_t$  for SF-Eel, Elder, and TR6 basins. Two potential scaling regimes were observed where the first regime extended from 20 m to the longest length of the tributary basin (20 m –  $L_{trimax}$ ). The documented scaling exponent for this regime is 1.55. The second potential scaling regime extended from 1 to 20 m where the observed scaling exponent was approximately 3. (b) The standard deviation of the tributary distance against the  $IAF_t$  for SF-Eel, Elder, and TR6 basins.

the order of the moment, i.e.,  $\tau(q) = qH$ . In contrast, if the singularity spectrum takes finite values on an interval  $[h_{max}, h_{min}]$ , the scaling exponents  $\tau(q)$  define a nonlinear function of  $q$ .

## 5. Results of Multiscale Analysis of IAFs

### 5.1. Results of Multithreshold Analysis of IAF: Distance Between Tributaries

Figure 5a shows results of the analysis of the average distance between tributaries ( $\langle d_{IAF_t} \rangle$ ) as a function of the IAF threshold ( $IAF_t$ ) for the SF-Eel, Elder, and TR6 basins. The bin sizes in the  $IAF_t$  used to compute  $d_{IAF_t}$  were varied from the smallest flow paths ( $\sim 1 \text{ m}^2$ ) to the largest tributary ( $\sim IAF_{max}$ ). The three basins analyzed in this work showed linear relationships in log-log space from the largest tributary basin to fairly small flow paths. The average distance ( $\langle d_{IAF_t} \rangle$ ) between these small flow paths was approximately 20 m (corresponding to  $IAF_t$  of  $\sim 1000 \text{ m}^2$ ), whereas the average distance between the largest tributaries was approximately equal to the distance between the two largest tributary basins ( $\delta L_{maxtrib}$ ) along the main

It is noted that the mother wavelet has at least one vanishing moment (by definition of wavelets), i.e.,  $\int \psi_0(x) dx = 0$ , acting thus as a differencing filter. However, by choosing wavelets with higher-order vanishing moments, i.e.,  $\int x^k \psi_0(x) dx = 0$  for  $0 \leq k \leq N - 1$  the removal of degree  $N$  polynomial trends from the signal is possible [e.g., Mallat, 1998]. A commonly used wavelet for multifractal analysis is the first- and second-order derivatives of a Gaussian function, defining thus generalized first- and second-order increments of the signal (e.g., see Figure 1 [Venugopal et al., 2006] for a plot of those wavelets).

Having computed the increments, or multiresolution coefficients  $\delta(x_0, a)$  of a signal, the next step is to compute the so-called partition function (or generalized structure function)  $S(q, a)$  defined as follows:

$$S(q, a) = \langle |\delta(x_0, a)^q| \rangle \quad (7)$$

where  $\langle . \rangle$  implies expectation. For a multifractal signal

$$S(q, a) \sim a^{\tau(q)} \quad (8)$$

which defines the  $\tau(q)$  curve, or spectrum of scaling exponents, indexed by the moment order  $q$ . The multifractal formalism states that  $\tau(q)$  and  $D(h)$  relate via a Legendre transform [e.g., Muzy et al., 1994]:

$$D(h) = \min_q [qh - \tau(q) + 1] \quad (9)$$

Note that if a signal is monofractal ( $D(h) = 1$  at  $h = H$  and zero everywhere else), the scaling exponents vary linearly with

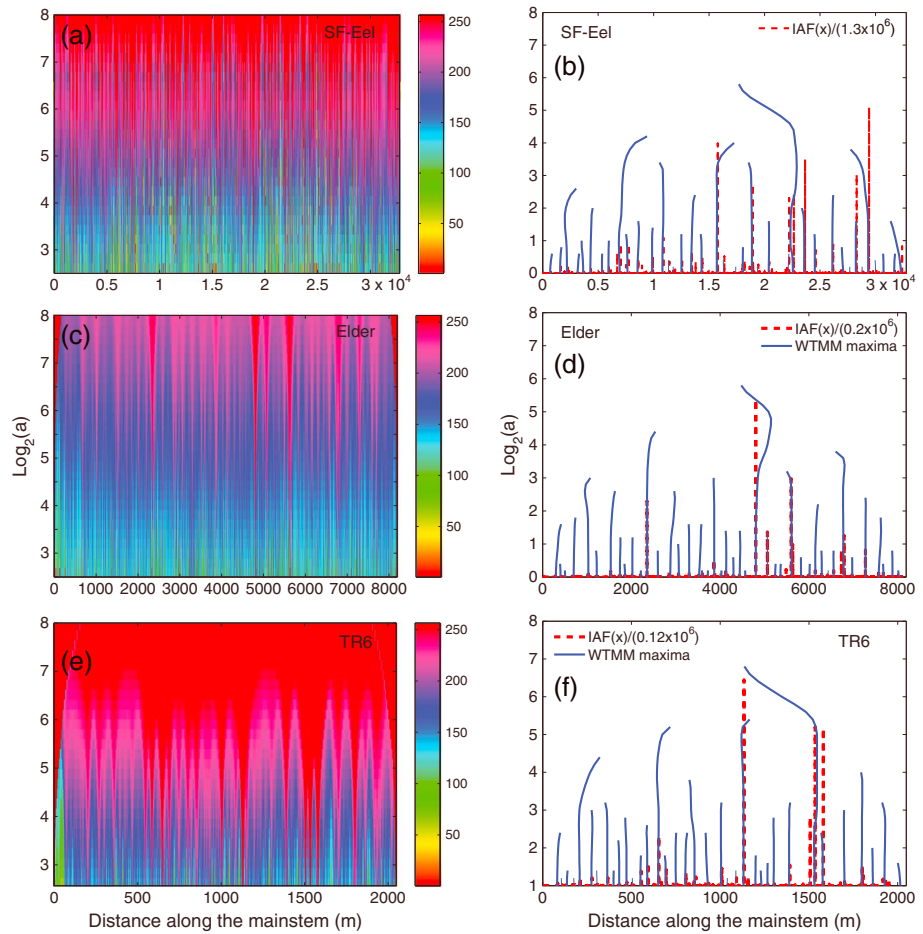


**Figure 6.** (a–f) Continuous wavelet transform (CWT) on the left and wavelet transform modulus maxima (WTMM) skeletons on the right for the IAFs of the South Fork Eel, Elder Creek, and TR6 basins. On the WTMM plots, rescaled IAFs by scale ratios of  $1.3 \times 10^6$ ,  $0.2 \times 10^6$ , and  $0.12 \times 10^6$  are superimposed. A limited range of scales is displayed to highlight the contribution of large tributaries. Red dashed lines in Figures 6b, 6d, and 6f show the scaled down version of IAFs at tributary junctions in three basins.

stem. For this scaling region, we found a simple power law scaling between  $\langle d_{IAF_t} \rangle$  and  $IAF_t$  where the observed scaling exponent was approximately 1.55. We also noted that there was a break in the relationship for scales less than 20 m in length (shown in dotted line) in all three basins. This scaling break is primarily due to the change of the probability distribution of  $d_{IAF_t}$  as the  $IAF_t$  reaches the scale of the entire hillslope (i.e.,  $IAF_t \sim 1000 \text{ m}^2$ ) [Rigon *et al.*, 1996]. A similar scaling behavior was observed for the standard deviations of the  $d_{IAF}$  versus  $IAF_t$  plot (Figure 5b) with scaling exponent (for the region extending from 20 m to  $\delta L_{\text{maxtrib}}$ ) approximately 2 for all basins.

### 5.2. Results of Multifractal Analysis

Before applying the wavelet-based methods for the estimation of the multifractal properties of the IAFs, it is instructive to visually inspect the continuous wavelet transform (CWT) and the wavelet transform modulus maxima (WTMM) of these functions. Figures 6a–6f show the CWT and the WTMM of the IAFs of the three analyzed basins. On the WTMM plots (Figures 6b, 6d, and 6f), the IAFs have been superimposed to illustrate how a large spike in the IAF contributes to a maxima line in the WTMM plot at that same point that has significant energy over a large range of scales (the WTMM line extends from small scales to very large scales). This is because the spikes associated with large tributaries are like Dirac deltas which need a broad range of frequencies to be represented. The CWT analysis computes at each scale the statistical moments of all the wavelet coefficients, while the WTMM analysis concentrates only on the wavelet coefficients on the maxima lines.

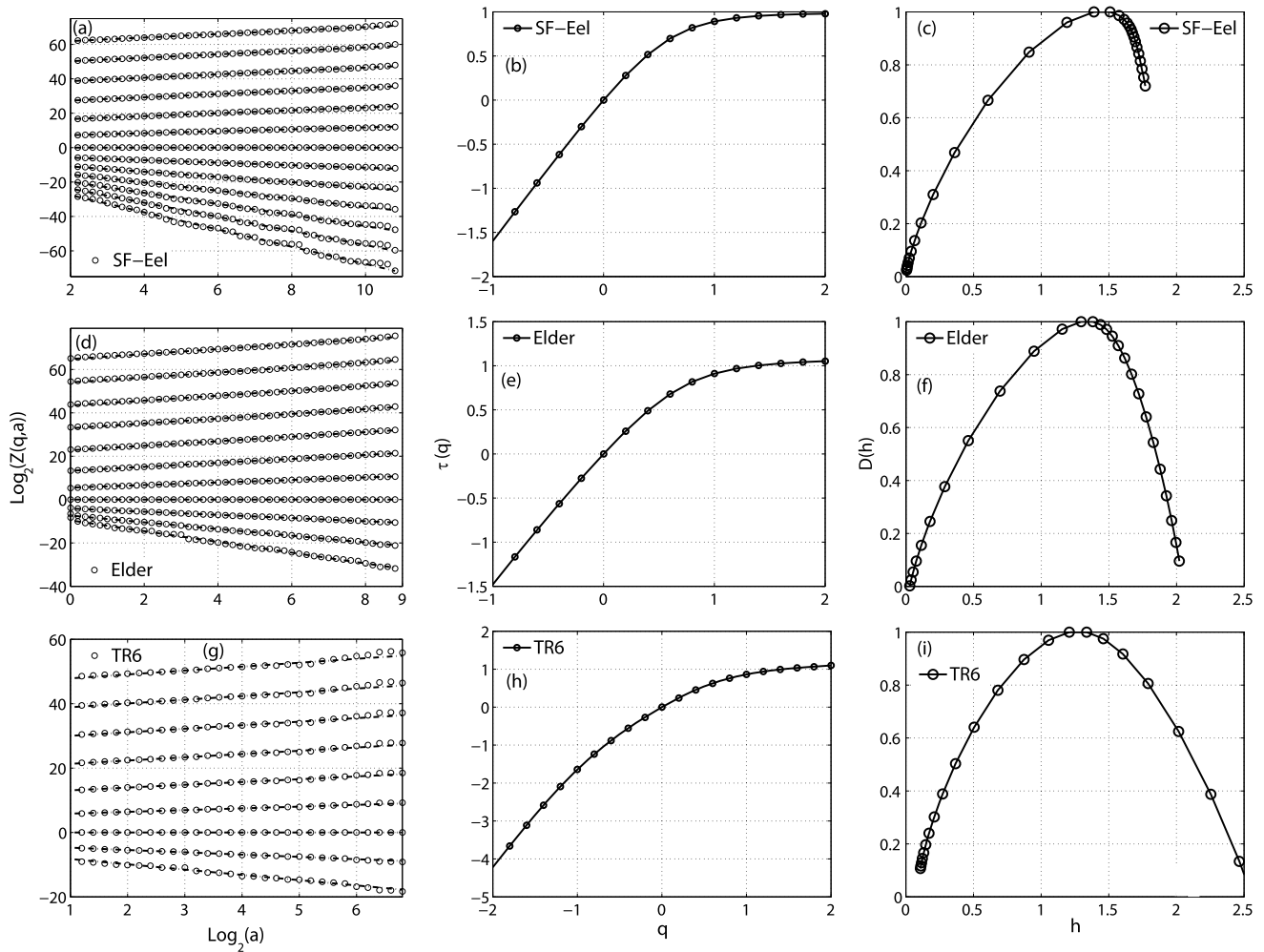


**Figure 7.** (a, d, and g) Partition functions (of order  $q = -3$  to  $3$  in increments of  $0.5$ ) versus scale in log-log plots computed using the WTMM confidants; (b, e, and h) the scaling exponents spectra ( $\tau(q)$ ); and (c, f, and i) the singularity spectrum  $D(h)$  for the three IAFs of main stems of South Fork Eel, Elder Creek, and TR6 basins (top to bottom).

Figures 7a, 7d, and 7g (left) show the log-log plots of the partition functions  $Z(q,a)$  as a function of scale  $a$ , for moment orders  $q = -3$  to  $q = +3$  in increments of  $0.5$ , computed from the WTMM coefficients. The slopes of those log-log plots (see Table 1 for the scaling ranges over which these slopes were estimated) have been computed and used to construct the  $\tau(q)$  versus  $q$  curves in Figures 7b, 7e, and 7h (middle column plots). Notice that the  $\tau(q)$  curve is a nonlinear function of  $q$ , thus implying multifractality. The Legendre transforms of the  $\tau(q)$  curves, which form the spectra of singularities  $D(h)$  curves, have been computed and are shown in Figures 7c, 7f, and 7i (right plots). We note that, similar to the concerns expressed in

**Table 1.** Multifractal Properties of the Incremental Area Function (IAF) for the South Fork Eel, Elder Creek, TR6 River Basins, and the Synthetic IAF<sup>a</sup>

Basin Name	Spectral Slope ( $\beta$ )	Main Stream Length (m)	Scaling Range (m)	Most Frequent $h$ ( $h_0$ )	( $h_{min}, h_{max}$ )	Intermittency Coefficient ( $c_2$ )
SF-Eel	2.02	56.6	2–1024	$1.46 \pm 0.02$	(0.00, 1.90)	$0.56 \pm 0.03$
Elder	2.05	11.2	2–512	$1.34 \pm 0.02$	(0.00, 2.00)	$0.58 \pm 0.03$
TR6	2.13	2.8	2–256	$1.27 \pm 0.02$	(0.00, 2.00)	$0.63 \pm 0.03$
Synthetic network	2.01	50.0	2–1024	1.30	(0.49, 1.80)	0.50

<sup>a</sup>Fourier Spectral Slope (cumulative IAF), main stem lengths, resulted scaling ranges, most frequent value of singularity exponent  $h_0$ , ( $h_{min}, h_{max}$ ) values, and intermittency coefficients for the three river basins are shown. The same variables are also shown for the synthetically generated IAF, which approximately agree with those of the real basins.

multifractal analysis of width and area functions [e.g., see *Lashermes and Fofoula-Georgiou, 2007; Veneziano et al., 2000*] we have paid special attention to possible edge effects and have repeated the analysis on a reduced signal from which the points close to the edges have been eliminated; no significant difference ( $\pm 0.02$  variation in the most frequently occurring singularity  $h_0$ , and  $\pm 0.03$  variation in  $c_2$ ) was observed in the estimated exponents.

Table 1 summarizes results of the multifractal analysis, namely, the scaling range, the most frequently occurring singularities (the value  $h_0$  at which the maximum of  $D(h)$  occurs),  $h_{\min}$  and  $h_{\max}$  as well as the coefficients  $c_1$  and  $c_2$  obtained by assuming a quadratic approximation of the  $\tau(q)$  curve, i.e.,  $\tau(q) = c_1 q + 1/2 c_2 q^2$ . In this sense,  $c_1$  is close to the value of  $h_0$  as it is dominated by the most frequently occurring singularity, and  $c_2$ , called the intermittency coefficient, depicts the spatial heterogeneity of the singularities (or the spread of the  $D(h)$  curve) at each tributary junction along the main stem.

It is interesting to note that the scaling range extends from scales of 2 m up to 1 km for the South Fork Eel River, 2 m to 0.5 km for Elder Creek, and 2 m to 0.25 km for TR6 basin. In TR6, the smallest basin, the scaling range extends over a length scale on the order of 1/10 of the main stem length, in the Elder Creek basin, 1/20 of the main stem length, and in the largest South Fork Eel River, the scaling range extends to a length scale on the order of 1/50 of the main stem length. This suggests that when the main stem length increases, the scaling range does not increase as fast (note that this ratio would be constant for subbasins of a perfectly fractal branching network). Generally, the shortening of the scaling range as a function of main stem length suggests that the larger basins are constrained by more anisotropic forcing, possibly arising from geological controls. It is also possible that this may be influenced by the fraction of the stream network that is dominated by hillslope (in the case of TR6 and Elder) versus fluvial processes (in the case of SF-Eel). The standard deviation of the  $d_{IAF_t}$  (Figure 5b) as a function of the threshold  $IAF_t$  shows larger variability in the SF-Eel River as compared to TR6 and Elder. This is especially so for distances between flow paths in the range of 1–20 m apart, possibly depicting different types of flow path drainage patterns and heterogeneities in those small scales as compared to the fluvial larger scales of the basin. A more systematic analysis of how the drainage patterns and length scales of flow paths in different erosional regimes, such as hillslope, colluvial, and fluvial regimes, might be needed to fully understand these anisotropic scaling of the IAF at different scales, something that falls beyond the analysis presented herein. For example, it would be expected for the IAF to demonstrate an unusual signature if different types of drainage patterns, such as purely dendritic and predominately parallel drainage networks are present within the basin (e.g., Roan Plateau, located in western Colorado, USA). Such heterogeneities may develop because different parts of the basin experience different forcing or because different parts of the basin simply respond differently to the same forcing (e.g., different lithologies may respond differently to the same tectonic forcing [*Castelltort et al., 2012*]). Such anisotropies may be represented in the IAF.

The estimated Hölder exponents range from zero (discontinuities at the location of very large tributaries) to approximately 2 (signifying a very smooth IAF at the locations of direct hillslope contributions). Interestingly, the most frequent Hölder exponent  $h_0$  and the intermittency coefficient  $c_2$  do not change significantly with the size of the basin, ranging between 1.27 to 1.47 and 0.63 to 0.56, respectively, for the three basins analyzed (smallest to largest). A lower  $h_0$  and a higher intermittency coefficient  $c_2$  is documented for the smallest TR6 basin, signifying a slightly more spatially heterogeneous nested tributary arrangement in that steeper basin. These results suggest that at larger scales there are natural tendencies toward particular topologies, but at finer scales there may be significant deviations from those expected topologies. An analysis of a larger number of subbasins may reveal systematic differences in the structure of the IAFs related to geology and other factors, which could form the basis of a classification scheme for concisely capturing the heterogeneity of tributary influence to the main stem fluxes of a river basin.

## 6. A Potential Cascade as Stochastic IAF Generator

Generating a measure or positive function that reproduces a desired multifractal spectrum has been the subject of considerable research over the past decade in a variety of fields, including turbulence, rainfall, and network topology [e.g., see *Schertzer and Lovejoy, 1987; Marani et al., 1991, 1994; Cârsteanu and Fofoula-Georgiou, 1996; Veneziano et al., 2000; Harris and Fofoula-Georgiou, 2001*, among others]. The most typical multifractal model is the multiplicative cascade which splits a mass from the initial support to smaller

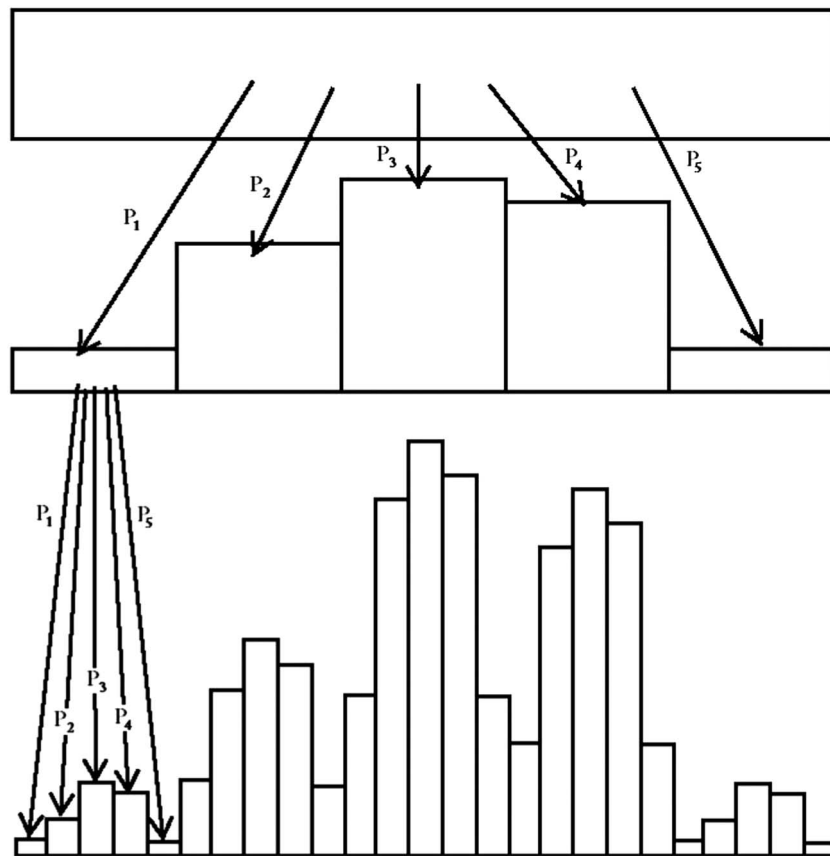


**Figure 8.** Schematic of pentanomial cascade used to model the incremental area function (IAF).

and smaller supports in a multiplicative manner using appropriately chosen weights. A binomial cascade which splits the mass dyadically is the most commonly used cascade. Such a generator, however, is not able to preserve specific desired features of a signal such as, for example, the build up (increasing intensity) and dissipating (decreasing intensity) stages of a storm [Venugopal *et al.*, 1999] or the specific form of the width function of a basin which has most of its mass concentrated in the middle part of the signal (due to the typical shape of river basins). Modifications of the typical cascade models have been proposed to incorporate such physically imposed features in a signal, such as the event-specific wavelet-based multiplicative cascade model proposed for rainfall by Cârsteanu *et al.* [1999] or the iterative random cascade proposed by Marani *et al.* [1994] or the iterative pulse model proposed by Veneziano *et al.* [2000] for width functions.

**Table 2.** The Probabilistic Mass of Each Interval of 0.2 Normalized Length From  $i = 0$  To 1 for South Fork Eel, Elder Creek, and TR6 Basins is Shown<sup>a</sup>

Basin	Probabilistic Mass in Each 0.2 Normalized Main Stem Length				
	0.0–0.2 ( $i = 1$ )	0.2–0.4 ( $i = 2$ )	0.4–0.6 ( $i = 3$ )	0.6–0.8 ( $i = 4$ )	0.8–1.0 ( $i = 5$ )
SF-Eel	0.12	0.20	0.28	0.33	0.07
Elder	0.06	0.18	0.30	0.32	0.10
TR6	0.05	0.22	0.36	0.34	0.14
Probability weight ( $p_i$ )	0.06	0.20	0.25	0.41	0.08

<sup>a</sup>The chosen weights for the deterministic cascade generation are shown in the last row. Each 0.2 normalized length increment from the ridge lines to the outlet are considered, and the average mass of each increment in all three basins is used to derive the probabilistic weight coefficient  $p_i$ . These weight coefficients are then used to generate the pentanomial cascade.

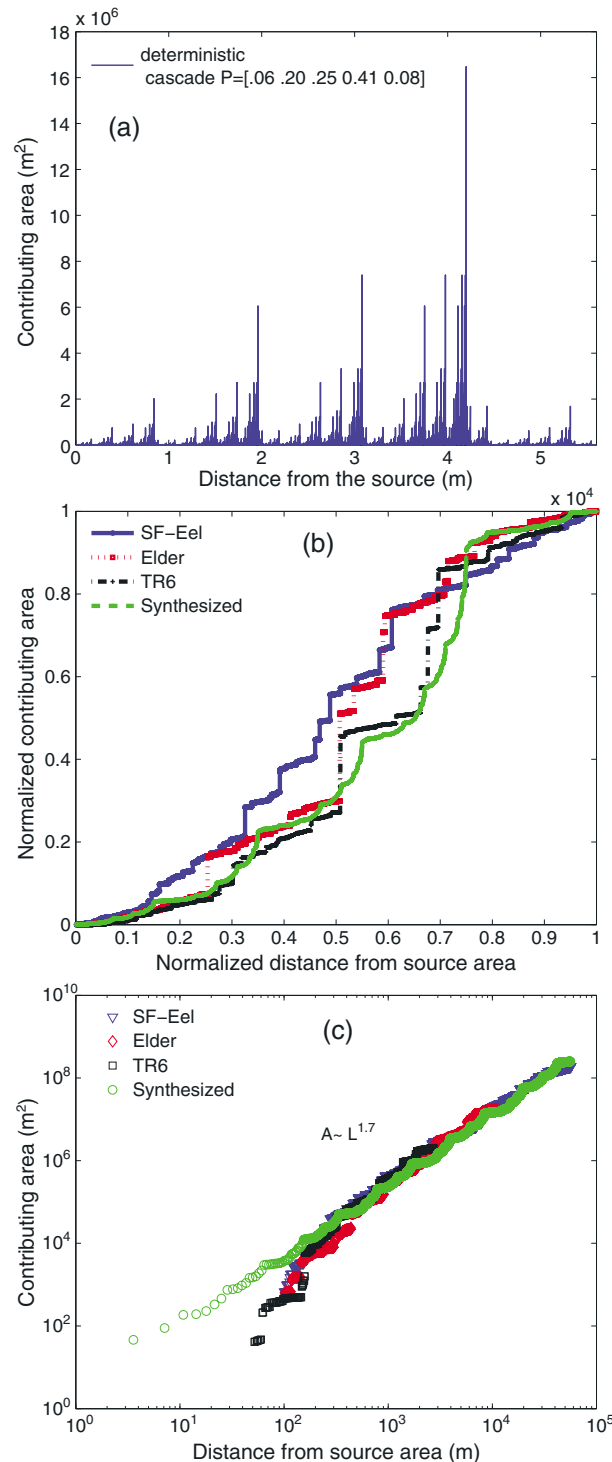


**Figure 9.** (a) IAF generated using a pentanomial cascade with weights  $p = [0.06; 0.20; 0.25; 0.41; 0.08]$ . (b) The cumulative area function of the synthesized IAF is compared with those of the SF-Eel, Elder Creek, and TR6 basins. (c) The contributing area of the synthesized IAF is plotted against the main stem length measured from source points in a log-log plot. The documented scaling exponent 1.7 agrees with the exponents of the three basins (SF-Eel, Elder, and TR6) for length scales corresponding to channelized parts of the river basins.

The constraint imposed by the IAF(x) structure on the stochastic generator is that no tributary basin entering the main stem at location  $x$  from the outlet can have length greater than  $x$  (if that were the case, the main stem would have to be redefined as to follow the longest flow path in the drainage basin). This constraint is not reproduced by a binary cascade generator. Here we propose the use of a pentanomial cascade (i.e., the support is split into five equal parts at every iteration; see schematic in Figure 8) whose weights are determined by the cumulative IAF(x) (Table 2). Note that increasing the order of the cascade generator would allow the contributing area to be more realistically approximated but would change the most frequent  $\langle H \rangle$  of the IAF fluctuations. We found that the pentanomial cascade is the most successful in reproducing  $\langle H \rangle$  in the IAF fluctuations for the river basins considered in this study. If we used a binomial cascade, the corresponding weight coefficients that would distribute the mass on the supports 0 to  $L/2$  and  $L/2$  to  $L$  are 0.4 and 0.6, respectively. The minimum  $h$  and maximum  $h$  ( $h_{\min} = \min(-\log_2(0.4, 0.6))$ ) and  $h_{\max} = \max(-\log_2(0.4, 0.6))$  for this configuration are 0.737 ( $h_{\min}$ ) and 1.329 ( $h_{\max}$ ). However, in the real basins we analyzed here that  $h_{\min}$  and  $h_{\max}$  were approximately 0.1 and 2.0, respectively. The pentanomial cascade that we used approximately reproduced the  $h_{\min}$  and  $h_{\max}$  as 0.5 and 1.8, respectively. The pentanomial cascade provides a better probability to have small as well as larger fluctuations for the IAF function than the binomial cascade. By using five coefficients, we can approximately distribute the contributing area well and reproduce the length constraint at tributary junctions in a realistic way. Further, binomial cascade does not realistically produce the very large and very small IAFs along the main stem as compared to pentanomial cascade.

We suggest deriving the weights of the pentanomial cascade as follows. The probability weights  $p$  at the  $i$ th interval,  $p_i$ , where  $i = 1:1:5$  (meaning from 1 to 5 in increments of 1) for each normalized length scale from 0 to 1 in intervals of 0.2 by dividing the incremental contributing area

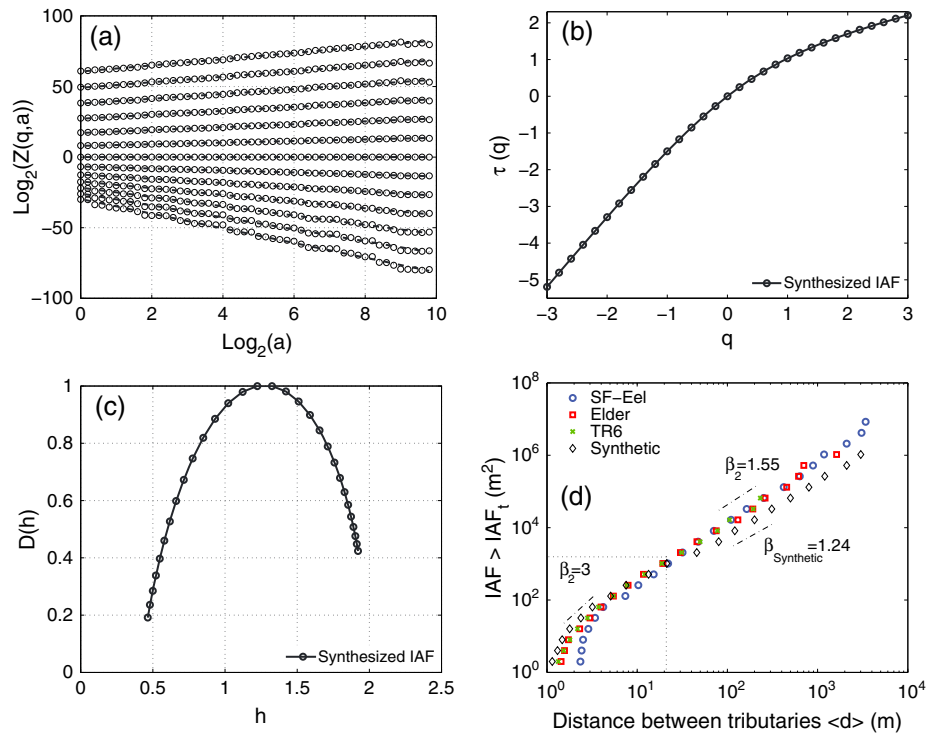


**Figure 10.** Multifractal properties of the synthetically generated IAF. A deterministic cascade with five bases and weights  $p = [0.06, 0.20, 0.25, 0.41, 0.08]$  was used for the synthetic IAF. Here shown are (a) partitioning function of order  $q = -3.0$  to  $3.0$  using CWT, (b) scaling exponents spectrum, (c) singularity spectrum, and (d) distance between tributaries for given area versus threshold contributing area.

at each interval,  $A(i) - A(i - 1)$ , by the total contributing area  $A_{\text{total}}$  (see Figure 2e). Note that  $A(0)$  equals zero and  $A(1)$  equals 1 (i.e.,  $p_1 = A(0.2)/A_{\text{total}}$ ,  $p_2 = (A(0.4) - A(0.2))/A_{\text{total}}$ ,  $p_3 = (A(0.6) - A(0.4))/A_{\text{total}}$ ,  $p_4 = (A(0.8) - A(0.6))/A_{\text{total}}$ , and  $p_5 = (A(1) - A(0.8))/A_{\text{total}}$ , where  $A(\cdot)$  denotes the total contributing area at normalized distance ( $\cdot$ ) from the outlet).

Figure 9a shows a MF signal generated by a pentanomial cascade with weights  $p = [0.06, 0.20, 0.25, 0.41, 0.08]$  (chosen in agreement with the cumulative area plot of the three basins; see Figure 2e). Figure 9b shows the cumulative area resulting from that cascade in relation to the cumulative areas of the three analyzed basins. It is observed that the deterministic pentanomial cascade is much more regular in appearance than the real IAFs, as expected. One more possibility is to randomize the weight selection criterion, which would allow very large masses to be randomly distributed while respecting the constraints imposed by the nested subbasins as has been applied for binomial cascades [Marani et al., 1994]. This is a subject of future research. Here, however, we demonstrate that this cascade reproduces the statistical properties of the IAFs. For example, the scaling (in terms of average drainage area) of the synthetic IAF and the real ones is shown in Figure 9c. As can be seen, the proposed model reproduces the average drainage area-length relationship of  $A \sim \ell^{1.7}$  observed in the real basins. The discrepancy between the generated cascade area-length relationship and those of the real basins for small scales (length scales smaller than 300 m) is to be expected because the exponent of 1.7 (Hack's law) is only valid within the channelized part of the river network. (Recall that in converting the areas to length scales in the previous section, the exponent 1.7 was used only for areas larger than  $A \geq 1 \times 10^{-1} \text{ km}^2$  which corresponds to length scales of the order of 300 m.)

In terms of higher-order moments (the full spectrum of singularities), it is noted that the proposed cascade is a multifractal with  $\tau(q)$  curve given as [Muzy et al., 1994] follows:

$$\tau(q) = \frac{\ln(p_1^q + p_2^q + \dots + p_5^q)}{\ln(\frac{1}{5})} \quad (10)$$

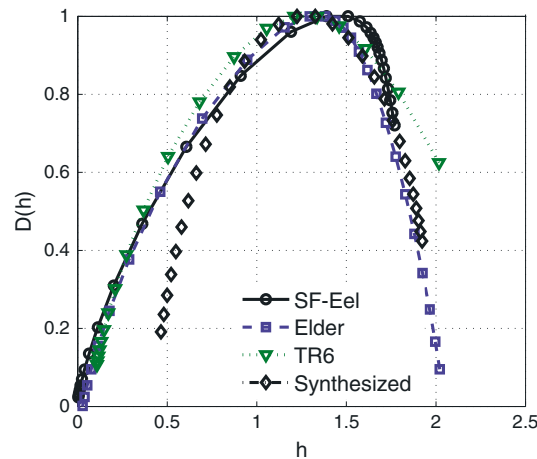


**Figure 11.** The singularity spectrum for the IAF of the three real basins (SF-Eel, Elder, and TR6) and of the synthetically generated IAF (using a pentanomial cascade with weights of 0.06, 0.20, 0.25, 0.41, and 0.08).

The support of the  $D(h)$  spectrum is in the interval  $[h_{\min}, h_{\max}]$  with  $h_{\min} = \min(-\log_5 p_i)$  and  $h_{\max} = \max(-\log_5 p_i)$ . It is noted that the pentanomial cascade provides flexibility in reproducing the minimum and maximum singularities  $h_{\min}, h_{\max}$  found in the IAFs by specifying the min and max weights of the cascade. Figure 10b shows the  $\tau(q)$  curve, the  $D(h)$  spectrum (Figure 10c), and the distance between tributaries for a given area versus threshold area (Figure 10d) for the synthetic IAF curve. A comparison of the  $D(h)$  curves of the three real basins and the synthetic IAF is seen in Figure 11. Notice that the synthetic IAF does not reproduce as well the small flow paths (minimum singularity) estimated from the real basin IAFs as the chosen maximum weight of 0.41 constrains the minimum singularity of the synthetic IAF to a value of approximately 0.5.

Further tuning of this IAF cascade generator, possibly using the method introduced in *Cârsteanu et al.* [1999] for detecting the branching structure of a cascade using WTMM and local extrema, is an issue that requires further study. Furthermore, we have shown that the IAF(x) can be converted to the width function. That suggests that we can synthetically generate the organization of the branching structure (width function) through IAF(x), and thus, we can generate width functions synthetically.

## 7. Discussion

The multithreshold decomposition of the IAF into different above-threshold series ( $IAF_t$ ), each representing a different scale in viewing the process, yielded a simple scaling power law relationship between the magnitude of the threshold  $IAF_t$  and the average separation distance  $\langle d_{IAF_t} \rangle$  of the incremental areas exceeding that threshold (i.e.,  $IAF_t \sim \langle d_{IAF_t} \rangle^{1.55}$ ). It is noted that the exponent 1.55 is approximately equal to the reciprocal of Hack's exponent (i.e.,  $A \sim \ell^{1.6}$ ). This scaling relationship was valid for length scales ranging from 20 m to  $L_{\max\text{trib}}$ , where  $L_{\max\text{trib}}$  is the distance between the two largest tributary basins along the main stem. The observed break in that relationship at the lower limit (i.e., distances less than 20 m) is indicative of the different topologic arrangements and different length scales of the small flow paths predominantly contributed to the main stem from adjacent hillslopes. Specifically, based on the finding from the multithreshold IAF analysis, it was concluded that the observed simple scaling relationship for the range from 20 m to  $L_{\max\text{trib}}$  arose from the organization of the distances between tributary basins and moderately large flow paths along the main streams. This result also suggested that the potential second scaling regime associated with 1–20 m scale arose mainly from the small flow path contributions, some of them possibly not fluvially dominated and thus having a different topologic and geometric structure. This suggests that fluvial regimes operate across a wide range of scales and therefore simple scaling analysis captures the precise scaling organization in an average sense (see also the results and discussion in *Convertino et al.* [2007]).

Our results on the statistical scaling of incremental area function (IAF) can be useful for up-scaling local field-based results to coarser scales. For example, IAF related fluxes (e.g., sediment flux and nutrient fluxes) observed at 1 m scale might need to be scaled nonlinearly by a scaling exponent of 3 to extrapolate to a 10 m length scale (i.e.,  $10^3$ ) if they scale exclusively as a function of area. In the same way, the observations made at larger scales ( $>20$  m) need to be scaled up by a scaling exponent of 1.55 to be extrapolated to longer lengths along the main stem. We emphasize here that the drainage density may vary broadly depending on the type of catchment and the dominant channel-forming processes. Besides, at the scales of interest, there may be only one (but notably more complex) scaling regime as documented by our multifractal analysis, and the success of simple scaling analyses in describing length-area relationships in river basins

stems precisely from the fact that the fluvial regime operates across scales several orders of magnitude, shadowing the smaller scales where the same regime might not be applicable. It is important to note that sediment and nutrient fluxes may not scale uniformly with area and thus IAF should be seen as just one step toward spatially distributed predictions of these fluxes. Further studies are needed to explore how IAF is related to these fluxes.

Wavelet based multiscale analysis yielded a scaling regime in which  $IAF(x) \sim x^H$ , where  $H$  varied from 1.27 to 1.47 and the scaling range extended from 2 to 1000 m. Higher-order statistical moments allow us to compute the whole spectrum of singularities (variation of the scaling exponent around the most frequent value  $h_0$ ) and reveal the statistical intermittency structure of  $IAF(x)$  resulting from tributaries of different size abruptly joining the main stream. Since we used 1 m lidar data, we analyzed 56,600 data points for the largest basin. For the smallest basin we analyzed 2800 data points. When the data size is larger than 1000 points, we were able to obtain a stable intermittency coefficient which was not depending on the data size. This suggests that even for the smallest basin (2800 data points), the intermittency coefficient we computed is stable.

In this work, we showed that a multiplicative cascade process can reproduce to a good accuracy the structure of the IAF signals we analyzed, so that it can be used as model for real basin IAFs. Specifically, the IAF signal we analyzed here was synthetically generated using a pentanomial cascade whose cascade weights were estimated from the IAF functions of the basins. The generated signal from the cascade had a spectrum of singularities with the most frequently occurring singularity  $h_0$  equal to 1.3, whereas the original signal had  $h_0$  approximately 1.4. This suggests that the IAF generated from the cascade approximately agrees with the multifractal properties shown by the IAF function (see Figures 10 and 11 for the distribution of Hölder exponents). Furthermore, Figure 10d shows the average distance between tributaries (for a given area) versus the thresholded area for the synthetically generated IAF. This was compared with the plots generated from three real basins (Figure 10d). As can be seen, the synthetically generated IAF showed a slope of 1.24, which is consistent with the slope shown by the three real basins analyzed in this study (Figure 10d). This slope is also consistent with the  $h_0$  we observed in the multifractal analyses for the synthetically generated IAF using the cascade approach (Figures 10c and 10d).

## 8. Concluding Remarks

Water and sediment flux as well as species abundance are predominantly associated with the distance between tributaries. Here we presented an analysis of the incremental area function  $IAF(x)$ , which presents a 1-D function that captures the two-dimensional hierarchical organization of a river basin (including hillslopes and nested tributaries) as mapped onto incremental areas draining along the main stem. As such, it documents the spatial heterogeneity in the drainage network structure within a river basin and gives more direct access to the hierarchical arrangement of larger and smaller tributaries as they alternate to contribute to the downstream fluxes in the main stem of a river basin.

In this paper, we quantified a simple power law relationship between a threshold incremental area ( $IAF_t$ ) and the average distance between tributaries exceeding that threshold ( $\langle d_{IAF_t} \rangle$ ) for three basins of a wide range of sizes (3 km<sup>2</sup> to 354 km<sup>2</sup>). We first characterized the scale invariance properties of the IAF and documented the presence of multiscaling. We observed that the average properties of IAF were consistent with Hack's law, but a pronounced degree of spatial heterogeneity in the clustering of tributaries entering the main stem was revealed, as documented via a wide spectrum of singularities. We also proposed a stochastic generator for the  $IAF(x)$  based on a pentanomial cascade with weights reflecting the general shape of the basin and discussed the need to introduce a structured stochasticity in the weight generator. Finally, we demonstrated that the  $IAF(x)$  and the width function  $W(x)$  of a basin can be directly related and that  $W(x)$  can be seen as a convolution of the  $IAF(x)$  with itself on the self-similar structure of a tree. Although in this study some differences were observed in the spatial heterogeneity of branching between very small (2 km<sup>2</sup>) and larger basins (250 km<sup>2</sup>), more analysis has to be undertaken to document systematic differences and size-dependence versus other climatic, geologic, and tectonic controls that determine landscape dissections.

## Appendix A: Estimation of $D(h)$ via WTMM

The correspondence between the  $\tau(q)$  curve and the  $D(h)$  function is established through the Legendre transform. From the Legendre transform, in the case of a continuously differentiable  $\tau(q)$ , it follows that

$$q = \frac{d}{dh}(D(h)) \quad (A1)$$

Thus, it is noted that the falling limb of  $D(h)$  (where  $\frac{d}{dh}(D(h)) < 0$ ) can only be estimated from the negative moments ( $q < 0$ ) of the fluctuations. However, computing negative statistical moments of probability density functions (pdfs) that have mass concentrated at zero (such as the pdfs of fluctuations) leads to a divergence problem [e.g., see Arneodo *et al.*, 1995]. To be able to compute negative statistical moments and estimate the complete singularity spectrum, Muzy *et al.* [1991, 1993] proposed to use the wavelet transform modulus maxima (WTMM) method, i.e., concentrate on the lines formed by following the maxima of the wavelet coefficients across scales and thus following the same singularity from the lowest scale to higher and higher scales. For details on this estimation, the reader is referred to the original publications [Muzy *et al.*, 1991, 1993; Arneodo *et al.*, 1998; Venugopal *et al.*, 2006]. As defined for the continuous wavelet transform (CWT), one can define a partition function  $Z(q, a)$  for the WTMM skeleton using its maxima lines as follows:

$$Z(q, a) = \sum_{\ell \in L(a)} |\tau_{\psi}[f](x, a)|^q \quad (A2)$$

where  $q$  is the moment order and  $L(a)$  is the set of all maxima lines  $\ell$  that satisfy

$$\ell \in L(a), \text{ if } \forall a' \leq a, \exists (x, a') \in \ell \quad (A3)$$

### Acknowledgments

We thank Collin Bode for providing us with the lidar data. Lidar data acquisition and processing were completed by the National Center for Airborne Laser Mapping (NCALM: <http://www.ncalm.org>). NCALM funding was provided by NSF's Division of Earth Sciences, Instrumentation and Facilities Program (EAR-1043051, 10.5069/G9639MPN). Lidar dataset used in this study are freely available at the following url: [http://opentopo.sdsc.edu/gridsphere/gridsphere?cid=geonlidarframeportlet&gs\\_action=datasetMetadata&otCollectionID=OT.022013.26910.1](http://opentopo.sdsc.edu/gridsphere/gridsphere?cid=geonlidarframeportlet&gs_action=datasetMetadata&otCollectionID=OT.022013.26910.1). Discussions throughout the course of this work with William Dietrich are greatly appreciated. This work has been partially supported by the National Center for Earth-surface Dynamics (NCED), a Science and Technology Center funded by NSF's Office of Integrative Activities under agreement EAR-0120914, an NSF CDI grant EAR-0835789, a Doctoral Dissertation Fellowship by the graduate school of the University of Minnesota, and the Ling Chair in Environmental Engineering to the senior author. Computer resources were provided by the Minnesota Supercomputing Institute, Digital Technology Center, at the University of Minnesota. We thank Andrea Rinaldo and Paolo Tarolli for their extremely helpful comments and thorough review of this paper. Finally, we would like to thank the Editor Alexander Densmore and Associate Editor John Pelletier for their valuable insight and comments on this work.

In other words, the summation at each scale  $a$  is done not over all points  $x$  but only over well-defined points that significantly contribute to the singularity at that point.

In this paper, the MF formalism is applied on the three IAFs using CWT and WTMM analyses. In implementing the WTMM estimation of  $D(h)$ , numerical instabilities that can arise when the maximum value of the modulus of the wavelet transform is very small and negative moments  $q$  are taken, divergence in the computation of  $Z(q, a)$  for negative values of  $q$  has been avoided by using the supremum (sup) values along the corresponding maxima lines. This method, called "WTMM with sup" is explained in detail in Venugopal *et al.* [2006]. Muzy *et al.* [1993], and Arneodo *et al.* [1998].

It is also noted that the inability of the WTMM with sup method to access negative singularities ( $h < 0$ ) (see section 2.4 of Venugopal *et al.* [2006] for details) can be circumvented by working with the cumulative (or integral) of the signal of interest. Since integration adds 1 to the singularities of the signal, i.e., it shifts  $D(h)$  to the right by 1, the singularities of the original signal can be recovered by shifting to the left by 1 the  $D(h)$  curve obtained by analysis of the cumulative signal.

### References

- Alexander, R. B., R. A. Smith, and G. E. Schwarz (2000), Effect of stream channel size on the delivery of nitrogen to the Gulf of Mexico, *Nature*, *403*, 758–761, doi:10.1038/35001562.
- Arneodo, A., E. Bacry, J. F. Muzy (1995), The thermodynamics of fractals revisited with wavelets, *Phys. A*, *213*(1–2), 232–275, ISSN 0378–4371, doi:10.1016/0378-4371(94)00163-N.
- Arneodo, A., E. Bacry, and J. F. Muzy (1998), Random cascades on wavelet dyadic trees, *J. Math. Phys.*, *39*(8), 4142–4164, doi:10.1063/1.532489.
- Banavar, J. R., J. Damuth, A. Maritan, and A. Rinaldo (2007), Scaling in ecosystems and the linkage of macroecological laws, *Phys. Rev. Lett.*, *98*(6), 068104, doi:10.1103/PhysRevLett.98.068104.
- Banavar, J. R., T. J. Cooke, A. Rinaldo, and A. Maritan (2014), Evolution and selection of river networks: Statics, dynamics, and complexity, *Proc. Natl. Acad. Sci. U.S.A.*, *111*(9), 3332–3337, doi:10.1073/pnas.1401336111.
- Beechie, T., and H. Imaki (2014), Predicting natural channel patterns based on landscape and geomorphic controls in the Columbia River basin, USA, *Water Resour. Res.*, *50*, 39–57, doi:10.1002/2013WR013629.
- Benda, L., K. Andras, D. Miller, and P. Bigelow (2004a), Confluence effects in rivers: Interactions of basin scale, network geometry, and disturbance regimes, *Water Resour. Res.*, *40*, W05402, doi:10.1029/2003WR002583.
- Benda, L., N. L. Po, D. Miller, T. Dunne, G. Reeves, G. Pess, and M. Pollock (2004b), The network dynamics hypothesis: How channel networks structure riverine habitats, *BioScience*, *54*(5), 413–427, doi:10.1641/0006-3568(2004)054[0413:TNDHHC]2.0.CO;2.
- Cărsteanu, A., and E. Foufoula-Georgiou (1996), Assessing dependence among weights in a multiplicative cascade model of temporal rainfall, *J. Geophys. Res.*, *101*(D21), 26,363–26,370, doi:10.1029/96JD01657.
- Cărsteanu, A., V. Venugopal, and E. Foufoula-Georgiou (1999), Event-specific multiplicative cascade models and an application to rainfall, *J. Geophys. Res.*, *104*(D24), 31,611–31,622, doi:10.1029/1999JD900388.

- Castellort, S., L. Goren, S. D. Willett, J. D. Champagnac, F. Herman, and J. Braun (2012), River drainage patterns in the New Zealand Alps primarily controlled by plate tectonic strain, *Nat. Geosci.*, *5*, 744–748, doi:10.1038/ngeo1582.
- Caylor, K. K., P. D'Odorico, and I. Rodriguez-Iturbe (2006), On the ecohydrology of structurally heterogeneous semiarid landscapes, *Water Resour. Res.*, *42*, W07424, doi:10.1029/2005WR004683.
- Convertino, M., R. Rigon, A. Maritan, I. Rodriguez-Iturbe, and A. Rinaldo (2007), Probabilistic structure of the distance between tributaries of given size in river networks, *Water Resour. Res.*, *43*, W11418, doi:10.1029/2007WR006176.
- Duncan, W. W., G. E. Poole, and J. Meyer (2007), Large channel confluences influence geomorphic heterogeneity of a southeastern United States river, *Water Resour. Res.*, *45*, W10405, doi:10.1029/2008WR007454.
- Feder, J. (1988), *Fractals*, 2nd ed., pp. 283, Plenum Press, New York.
- Ferguson, R. I., J. R. Cuddenn, T. B. Hoey, and S. P. Rice (2006), River system discontinuities due to lateral inputs: Generic styles and controls, *Earth Surf. Processes Landforms*, *31*, 1149–1166, doi:10.1002/esp.1309.
- Foster, M. A., and H. M. Kelsey (2012), Knickpoint and knickzone formation and propagation, South Fork Eel River, Northern California, *Geosphere*, *8*(2), 403–416, doi:10.1130/GES00700.1.
- Fuller, T. K., L. A. Perg, J. K. Willenbring, and K. Lepper (2009), Field evidence for climate-driven changes in sediment supply leading to strath terrace formation, *Geology*, *37*(5), 467–470, doi:10.1130/G25487A.1.
- Gangodagamage, C. (2009), Scale invariance and scaling breaks—New metrics for inferring process signature from high resolution lidar topography, PhD dissertation, 132 pp., Univ. of Minnesota, Minneapolis. [Available at <http://hdl.handle.net/11299/57133>, 31 October.]
- Gangodagamage, C., E. Barnes, and E. Fofoula-Georgiou (2007), Scaling in river corridor widths depicts organization in valley morphology, *Geomorphology*, *91*(3–4), 198–215, doi:10.1016/j.geomorph.2007.04.014.
- Gangodagamage, C., C. X. Zhou, and H. S. Lin (2008), Spatial autocorrelation, in *Encyclopedia of GIS*, edited by S. Shekhar and H. Xiong, pp. 32–37, Springer, N. Y., doi:10.1007/978-0-387-35973-1\_83. [Available at <http://refworks.springer.com/geograph>.]
- Gangodagamage, C., P. Belmont, and E. Fofoula-Georgiou (2011), Revisiting scaling laws in river basins: New considerations across hillslope and fluvial regimes, *Water Resour. Res.*, *47*, W07508, doi:10.1029/2010WR009252.
- Gangodagamage, C., et al. (2014), Extrapolating active layer thickness measurements across arctic polygonal terrain using lidar and NDVI datasets, *Water Resour. Res.*, *50*, 6339–6357, doi:10.1002/2013WR014283.
- Hack, J. (1957), *Studies of Longitudinal Profiles in Virginia and Maryland, U.S.*, Geol. Surv. Prof. Pap., pp. 294-B, U.S. Govt. Print. Off., Wash.
- Harris, D., and E. Fofoula-Georgiou (2001), Subgrid variability and stochastic downscaling of modeled clouds: Effects on radiative transfer computations for rainfall retrieval, *J. Geophys. Res.*, *106*(D10), 10,349–10,362, doi:10.1029/2000JD900797.
- Hutchinson, M. (1989), A new procedure for gridding elevation and stream line data with automatic removal of spurious pits, *J. Hydrol.*, *106*, 211–232, doi:10.1016/0022-1694(89)90073-5.
- Jencso, K. G., and B. L. McGlynn (2011), Hierarchical controls on runoff generation: Topographically driven hydrologic connectivity, geology, and vegetation, *Water Resour. Res.*, *47*, W11527, doi:10.1029/2011WR010666.
- Jennings, C. W., and R. G. Strand (1960), Geologic map of California, Ukiah sheet: California Division of Mines and Geology, scale 1:250,000.
- Jenson, S., and J. Domingue (1988), Extracting topographic structure from digital elevation data for geographic information system analysis, *Photogramm. Eng. Remote Sens.*, *54*(11), 1593–1600.
- Kelsey, H. M., and G. A. Carver (1988), Late Neogene and Quaternary tectonics associated with northward growth of the San Andreas Transform Fault, Northern California, *J. Geophys. Res.*, *93*(B5), 4797–4819, doi:10.1029/JB093iB05p04797.
- Kiney, P. M., C. M. Greene, J. E. Hall, and J. R. Davies (2006), Tributary streams create spatial discontinuities in habitat, biological productivity, and diversity in mainstem rivers, *Can. J. Fish Aquat. Sci.*, *63*(11), 2518–2530, doi:10.1139/f06-138.
- Kirchner, J. W., and C. Neal (2013), Universal fractal scaling in stream chemistry and its implications for solute transport and water quality trend detection, *Proc. Natl. Acad. Sci. U.S.A.*, doi:10.1073/pnas.1304328110.
- Lashermes, B., and E. Fofoula-Georgiou (2007), Area and width functions of river networks: New results on multifractal properties, *Water Resour. Res.*, *43*, W09405, doi:10.1029/2006WR005329.
- Mallat, S. (1998), *A Wavelet Tour of Signal Processing*, 2nd ed., pp. 840, Academic Press, San Diego, Calif.
- Marani, A., R. Rigon, and A. Rinaldo (1991), A note on fractal channel networks, *Water Resour. Res.*, *27*(12), 3041–3049, doi:10.1029/91WR02077.
- Marani, M., A. Rinaldo, R. Rigon, and I. Rodriguez-Iturbe (1994), Geomorphological width functions and the random cascade, *Geophys. Res. Lett.*, *21*, 2123–2126, doi:10.1029/94GL01933.
- Muneepeerakul, R., A. Rinaldo, and I. Rodriguez-Iturbe (2007a), Effects of river flow scaling properties on riparian width and vegetation biomass, *Water Resour. Res.*, *43*, W12406, doi:10.1029/2007WR006100.
- Muneepeerakul, R., L. A. Levin, A. Rinaldo, and I. Rodriguez-Iturbe (2007b), On biodiversity in river networks: A trade-off metapopulation model and comparative analysis, *Water Resour. Res.*, *43*, W07326, doi:10.1029/2006WR005857.
- Muneepeerakul, R., E. Bertuzzo, H. J. Lynch, W. F. Fagan, A. Rinaldo, and I. Rodriguez-Iturbe (2008), Neutral metacommunity models predict fish diversity patterns in Mississippi-Missouri basin, *Nature*, *453*, 220–222, doi:10.1038/nature06813.
- Muzy, J., E. Bacry, and A. Arneodo (1991), Wavelets and multifractal formalism for singular signals: Application to turbulence data, *Phys. Rev. Lett.*, *67*, 3515–3518, doi:10.1103/PhysRevLett.67.3515.
- Muzy, J., E. Bacry, and A. Arneodo (1993), Multifractal formalism for fractal signals: The structure-function approach versus the wavelet-transform modulus-maxima method, *Phys. Rev. E*, *47*(2), 875–884, doi:10.1103/PhysRevE.47.875.
- Muzy, J., E. Bacry, and A. Arneodo (1994), The multifractal formalism revisited with wavelets, *Int. J. Bifurcation Chaos*, *4*(2), 245–302, doi:10.1142/S0218127494000204.
- O'Callaghan, J., and D. Mark (1984), The extraction of channel networks from digital elevation data, *Comput. Vis. Graph. Image Process.*, *28*, 328–344.
- Power, M. E. (1992), Habitat heterogeneity and the functional significance of fish in river food webs, *Ecology*, *73*(5), 1675–1688, doi:10.2307/1940019.
- Reiger, W. (1998), A phenomenon-based approach to upslope contributing area and depressions in DEMs, *Hydrol. Process.*, *12*(6), 857–872, doi:10.1002/(SICI)1099-1085(199805)12.
- Rice, S. (1998), Which tributaries disrupt downstream fining along gravel-bed rivers?, *Geomorphology*, *22*(1), 39–56, doi:10.1016/S0169-555X(97)00052-4.
- Rice, S. P., B. L. Rhoads, and A. G. Roy (2008), Introduction: River confluences, tributaries and the fluvial network, in *River Confluences, Tributaries and the Fluvial Network*, edited by S. P. Rice, A. G. Roy, and B. L. Rhoads, John Wiley, Chichester, U. K., doi:10.1002/9780470760383.ch1.
- Richards-Pecou, B. (2002), Scale invariance analysis of channel network width function and possible implications for flood behavior, *Hydrol. Sci. J.*, *47*(3), 387–404.

- Rigon, R., I. Rodriguez-Iturbe, A. Maritan, A. Giacometti, D. G. Tarboton, and A. Rinaldo (1996), On Hack's law, *Water Resour. Res.*, 32(11), 3367–3374, doi:10.1029/96WR02397.
- Rinaldo, A., A. Marani, and R. Rigon (1991), Geomorphological dispersion, *Water Resour. Res.*, 27(4), 513–525, doi:10.1029/90WR02501.
- Rinaldo, A., R. Rigon, J. R. Banavar, A. Maritan, and I. Rodriguez-Iturbe (2014), Evolution and selection of river networks: Statics, dynamics, and complexity, *Proc. Natl. Acad. Sci. U.S.A.*, 111(7), 2417–2424, doi:10.1073/pnas.1322700111.
- Riveros-Iregui, D. A., B. L. McGlynn, L. A. Marshall, D. L. Welsch, R. E. Emanuel, and H. E. Epstein (2011), A watershed-scale assessment of a process soil CO<sub>2</sub> production and efflux model, *Water Resour. Res.*, 47, W00J04, doi:10.1029/2010WR009941.
- Rodriguez-Iturbe, I., and A. Rinaldo (1997), *Fractal River Networks: Chance and Self-Organization*, 540 pp., Cambridge Univ. Press, New York.
- Rodriguez-Iturbe, I., R. Muneeppeerakul, E. Bertuzzo, S. A. Levin, and A. Rinaldo (2009), River networks as ecological corridors: A complex systems perspective for integrating hydrologic, geomorphologic, and ecologic dynamics, *Water Resour. Res.*, 45, W01413, doi:10.1029/2008WR007124.
- Saco, P. M., and P. Kumar (2002), Kinematic dispersion in stream networks: 2. Scale issues and self-similar network organization, *Water Resour. Res.*, 38(11), 1245, doi:10.1029/2001WR000694.
- Schertzer, D., and S. Lovejoy (1987), Physical modeling and analysis of rain and clouds by anisotropic scaling multiplicative processes, *J. Geophys. Res.*, 92(D8), 9693–9714, doi:10.1029/JD092iD08p09693.
- Schroeder, M. (1991), *Fractals, Chaos, Power Laws: Minutes From an Infinite Paradise*, W. H. Freeman, New York.
- Seidl, M. A., and W. E. Dietrich (1992), The problem of channel erosion into bedrock, *Catena Suppl.*, 23, 101–124.
- Snell, J. D., and M. Sivapalan (1994), On geomorphological dispersion in natural catchments and the geomorphological unit hydrograph, *Water Resour. Res.*, 30(7), 2311–2323, doi:10.1029/94WR00537.
- Strand, R. G. (1962), Geologic map of California, Redding sheet: California division of mines and geology, scale 1:250,000.
- Tarboton, D. G. (1997), A new method for the determination of flow directions and upslope areas in grid digital elevation models, *Water Resour. Res.*, 33(2), 309–319, doi:10.1029/96WR03137.
- Tarolli, P. (2014), High-resolution topography for understanding Earth surface processes: Opportunities and challenges, *Geomorphology*, 216, 295–312, doi:10.1016/j.geomorph.2014.03.008.
- Veneziano, D., G. E. Moglen, P. Furcolo, and V. Iacobellis (2000), Stochastic model of the width function, *Water Resour. Res.*, 36(4), 1143–1157, doi:10.1029/2000WR900002.
- Venugopal, V., E. Foufoula-Georgiou, and V. Sapozhnikov (1999), Evidence of dynamic scaling in space-time rainfall, *J. Geophys. Res.*, 104(D24), 31,599–31,610, doi:10.1029/1999JD900437.
- Venugopal V., S. G. Roux, E. Foufoula-Georgiou, A. Arnéodo (2006), Scaling behavior of high resolution temporal rainfall: New insights from a wavelet-based cumulant analysis, *Phys. Lett. A*, 348(3–6), 335–345, ISSN 0375–9601, doi:10.1016/j.physleta.2005.08.064.
- Ward, J. V., K. Tockner, D. B. Arscott, and C. Claret (2002), Riverine landscape diversity, *Freshwater Biol.*, 47(4), 517–539, doi:10.1046/j.1365-2427.2002.00893.x.
- Wiens, J. A. (2002), Riverine landscapes: Taking landscape ecology into the water, *Freshwater Biol.*, 47(4), 501–515, doi:10.1046/j.1365-2427.2002.00893.x.D.